

# Shear layer response to overmodulated acoustic perturbations <sup>F</sup>


Cite as: Phys. Fluids **35**, 015113 (2023); <https://doi.org/10.1063/5.0130336>

Submitted: 11 October 2022 • Accepted: 12 December 2022 • Accepted Manuscript Online: 13 December 2022 • Published Online: 05 January 2023

Published open access through an agreement with JISC Collections

 C. J. Nicholls,  K. Chakravarthy,  B. M. T. Tang, et al.

## COLLECTIONS

 This paper was selected as Featured



View Online



Export Citation



CrossMark

## ARTICLES YOU MAY BE INTERESTED IN

[On acoustically modulated jet shear layers and the Nyquist-Shannon sampling theorem](#)

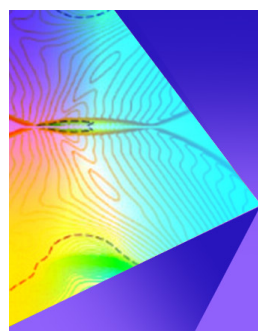
Physics of Fluids **34**, 115106 (2022); <https://doi.org/10.1063/5.0118025>

[Large eddy simulation of ship airflow control with steady Coanda effect](#)

Physics of Fluids **35**, 015112 (2023); <https://doi.org/10.1063/5.0127560>

[A phenomenological analysis of droplet shock-induced cavitation using a multiphase modeling approach](#)

Physics of Fluids **35**, 013312 (2023); <https://doi.org/10.1063/5.0127105>



## Physics of Fluids

## Special Topic: Shock Waves

**Submit Today!**

# Shear layer response to overmodulated acoustic perturbations

Cite as: Phys. Fluids **35**, 015113 (2023); doi: [10.1063/5.0130336](https://doi.org/10.1063/5.0130336)

Submitted: 11 October 2022 · Accepted: 12 December 2022 ·

Published Online: 5 January 2023



View Online



Export Citation



CrossMark

C. J. Nicholls,<sup>a)</sup>  K. Chakravarthy,  B. M. T. Tang,  B. A. O. Williams,  and M. Bacic 

## AFFILIATIONS

Department of Engineering Science, University of Oxford, Oxford OX2 0ES, United Kingdom

<sup>a)</sup> Author to whom correspondence should be addressed: [christopher.nicholls@eng.ox.ac.uk](mailto:christopher.nicholls@eng.ox.ac.uk)

## ABSTRACT

Shear layers act as demodulators when subjected to amplitude modulated, acoustic perturbations. Recent work explained that the demodulation is a result of the hypothesized relationship between the excitation waveform and the vorticity signal of the large-scale structures, which was represented by a half-wave rectification model. In this paper, this model is explored by overmodulating the excitation signal amplitude. The rectifier model predicts several effects of overmodulation on the flow response, including a doubling of the demodulated response frequency. To validate these predictions, a free, round jet that is excited acoustically upstream of the nozzle is studied using particle image velocimetry. Analytical results from the model are confirmed using a second experimental setup where a jet that emerges from a nozzle and attaches to an adjacent, inclined wall is excited acoustically. Beyond the insight it provides into shear layer vortex dynamics, overmodulation serves as a useful excitation technique for practical applications, where the shear layer response frequency can be increased at the expense of the response amplitude.

© 2023 Author(s). All article content, except where otherwise noted, is licensed under a Creative Commons Attribution (CC BY) license (<http://creativecommons.org/licenses/by/4.0/>). <https://doi.org/10.1063/5.0130336>

## I. INTRODUCTION

When a shear layer is excited with a harmonic perturbation of sufficient strength, vortices are rolled up and shed at the excitation frequency.<sup>1</sup> Assuming a fixed perturbation frequency, the perturbation amplitude determines the size and strength of the vortices produced and hence the degree to which mixing across the shear layer is enhanced.<sup>2</sup> In the case of jet shear layers, the perturbation amplitude therefore determines the degree of additional jet spreading. If the amplitude is modulated, the shear layer responds at the modulating signal frequency and hence acts as a demodulator.<sup>3</sup> Numerous flow control studies have harnessed this technique in applications like boundary layer control,<sup>4</sup> piezo-fluidic device control,<sup>5,6</sup> and jet thrust vectoring.<sup>7,8</sup> Yehoshua and Seifert<sup>9</sup> also reported the demodulation effect in synthetic jet actuators.

Several studies have demonstrated that vortex merging is a mechanism for demodulation. Wiltse and Glezer<sup>3</sup> used piezoelectric actuators to excite the flow in a square conduit. Using Schlieren photography, they illustrated that line vortices were created at the carrier frequency,  $f_c$ , which merged into vortices at the modulating frequency,  $f_m$ , some distance downstream. Vukasinovic *et al.*<sup>10</sup> studied the use of a synthetic jet actuator to control the separation of the flow over a backward-facing step using particle image velocimetry (PIV).

When the excitation waveform was an amplitude-modulation (AM) signal, vortices were produced at the carrier frequency,  $f_c$ , and rolled up into larger vortices at the modulating frequency,  $f_m$ . Yehoshua and Seifert<sup>9</sup> explained the mechanism by which synthetic jet actuators demodulate AM signals. The vortices were produced at the carrier frequency and their strength varied at the modulating signal frequency. Vortices produced when the modulating signal was below a certain threshold were re-ingested by the synthetic jet on the intake stroke. Vortices strong enough to escape the synthetic jet underwent merging events to produce a single vortex per modulating signal period,  $1/f_m$ , sufficiently far downstream.

Nicholls *et al.*<sup>2</sup> demonstrated that vortex merging is not always required for demodulation and represents one of two mechanisms. The other mechanism is based on the fact that the vortex strengths vary with the modulating signal and that the corresponding vorticity signal resembles a half-wave rectified version of the AM excitation waveform—a common implementation of a demodulator in communication systems (Ref. 11, p.157). We also introduced the notion that the vortices “sample” the modulating signal during the time they are created to determine their strength, and analogies from signal processing can be used to describe their behavior. The vortices behave like the samples of a digital control system, and the corollary is that the

Nyquist–Shannon sampling theorem<sup>12</sup> applies when the modulating frequency,  $f_m$ , exceeds half the vortex generation frequency, that is, the carrier frequency,  $f_c$ . In the present work, the modulating frequency is kept below half the carrier frequency ( $f_m < f_c/2$ ) to avoid this aliasing effect.

In this paper, we adopt the signal processing perspective developed by Nicholls *et al.*<sup>2</sup> to investigate the effects of overmodulated acoustic excitation on jet shear layer behavior. Principally, we seek to explore the half-wave rectification model proposed in Nicholls *et al.*<sup>2</sup> and provide insight into shear layer vortex dynamics through analysis and experiments. We further demonstrate that overmodulation in the context of acoustically excited fluid flows has merit as an excitation technique for practical applications.

A canonical, free, round jet is studied using particle image velocimetry (PIV) where the acoustic excitation is introduced upstream of the nozzle. To investigate the spectral response and compare it with the analytical prediction, a second experimental setup is used in which a jet emerges from a nozzle and attaches to an adjacent, inclined wall. In this experiment, the acoustic excitation is directed at the jet in a transverse direction from the unattached side at the point where it emerges from the nozzle. The jet position, as measured by a pitot probe downstream, is used as a proxy for the degree of jet spreading and hence the shear layer response. The goal is to understand the shear layer response through the lens of the jet response, which is the measured variable. The purpose of this experiment is to make a quantitative assessment of the effect of overmodulating the input excitation for comparison with the predictions from the analysis of the model. It also represents a practical application where overmodulated excitation may be useful, in this case to control the degree of separation of a reattaching jet.

The signal processing perspective on the jet response to modulated perturbations is outlined in Sec. III after the experimental methods are described in Sec. II. The results from both experiments are presented in Secs. IV and V. A discussion is provided in Sec. VI, before a summary and conclusions are given in Sec. VII.

## II. EXPERIMENTAL METHODS

### A. Free jet

The experimental setup is the same as in Nicholls *et al.*<sup>2</sup> The free, round jet test section is reproduced in Fig. 1. An air jet emerges from a nozzle into an acrylic box with two outlets on the opposite face. These outlets are joined by flexible hose and connected to a building exhaust

system, which provides a small back pressure to the flow. The nozzle has a 7.5-mm-diameter circular cross section and is 165 mm long. The hole in the box through which the nozzle supplies the flow was drilled off-perpendicular such that the jet is not completely straight. The extent of the jet angle is apparent in the baseline data presented in Sec. IV. The flow is excited by a loudspeaker upstream of the nozzle in a plenum, with the loudspeaker (the 10 W Visaton FR 58) directed perpendicularly to the streamwise direction. The loudspeaker is driven by a power amplifier (40 W Kemo Electronic M034N), which is connected to a signal generator. The flow is seeded with di-ethyl-hexyl-sebacate (DEHS) using a LaVision aerosol generator. The droplet size ranges between 0.1 and 1  $\mu$  m. The particle density and flow rate are controlled by two mass flow controllers (both Omega FMA-2612A) and a bypass route, both upstream of the test section and supplied by a lab ring-main air supply. The mass flow controllers have a combined error of  $\pm 2.8\%$  in the mass flow rate. The light sheet from a dual-head Nd:YAG New Wave Gemini PIV 200–15 laser that produces a beam at 532 nm with 14 mJ per pulse is used to reproduce the velocity vector field of the jet from the nozzle orifice to around eight nozzle widths downstream. The laser is passed through cylindrical and spherical lenses of focal lengths 90 and 350 mm, respectively, to form it into a sheet less than 0.5 mm thick and 2.5 nozzle widths wide. Image pairs are acquired using a charge-coupled device (CCD) camera (Bobcat B1621M) with a fixed inter-frame time of 200 ns. A calibration grid is used to set the focus, correct for optical distortion, and scale the vector units to m/s.

The laser inter-pulse time is set to 10.5  $\mu$ s. A standard, decreasing window size, multipass processing scheme is used to calculate the velocity vector field. The three passes use  $128 \times 128$ ,  $64 \times 64$ , and  $32 \times 32$  pixel interrogation window sizes. Spatial resolution is improved through the use of an overlap of 50% for all passes. The resulting discretization of the flow field is a grid with a spacing of 0.08 nozzle widths between stations. A vector-validation filter is used that removes anomalous vectors that exceed a predetermined range and interpolates the surrounding vector field to replace them. The Stokes number based on the maximum particle size, the nozzle diameter, and the average nozzle velocity is below 0.01. Errors associated with tracing accuracy are therefore bounded to be less than 1%. The laser and camera are triggered at 10 Hz so that events occurring at multiples of 10 Hz are aliased onto DC. The trigger generator does not time the signal generator, and consequently, the input waveform phase is not known relative to the phase of the measurements. Scatter from the

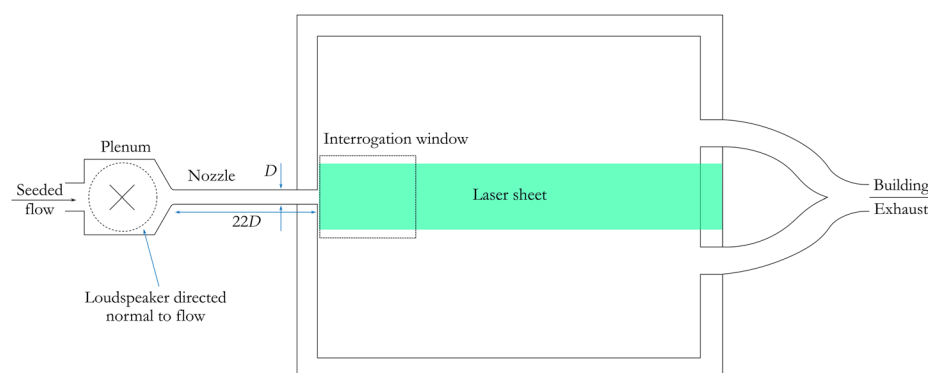


**FIG. 1.** Free jet test section setup, reproduced with permission from Nicholls *et al.*, Phys. Fluids 34, 115106 (2022). Copyright 2022 AIP Publishing. (a) Labeled diverging channel diagram. (b) Dimensioned diverging channel diagram.

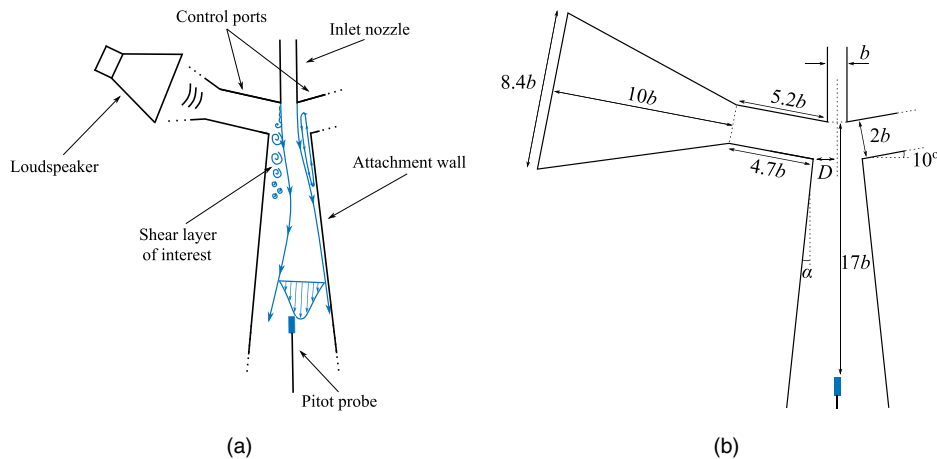


FIG. 2. Flow configuration—diverging channel with reattaching jet.

nozzle corrupts the measurements in a narrow region immediately downstream of the nozzle approximately  $0.1D$  long. The flow rate used was  $1.06 \text{ g/s}$  for all free jet experiments, with an accumulated uncertainty of  $2.8\%$  in the mass flow controllers. The jet has a (measured) mean velocity of  $20.3 \pm 0.2 \text{ m/s}$ , implying a density of  $1.19 \pm 0.05 \text{ kg/m}^3$ . This corresponds to a Reynolds number based on jet diameter given by  $\text{Re}_D = uD/\nu \approx 10^4$ .

### B. Attached jet

The shear layer studied in the second experimental setup is on the unattached side of a reattaching jet in a diverging channel (Fig. 2). A photograph of the test section is shown in Fig. 3. The wall angle in the diverging section is  $\alpha = 6^\circ$ , the nozzle has a rectangular cross section with width  $b = 5 \text{ mm}$  and depth  $d = 15 \text{ mm}$ , and the initial wall setback is  $D = 1.99b$ . The wall angle used is not important for the purpose of demonstrating the effect of an over-modulated excitation waveform. A pitot probe (Kulite XCQ series pressure transducer) on the device centerline,  $17$  nozzle widths downstream of the orifice, is sampled at  $50 \text{ kHz}$  via a first-order,  $25 \text{ kHz}$  anti-aliasing filter. The blockage ratio of the pitot probe in the channel, defined as  $A_r = A_p/A_{ch}$ , where  $A_p$  is the probe area and  $A_{ch}$  is the smallest area of the diverging channel where the probe is, that is, the worst-case blockage, takes the value  $A_r = 1.5\%$ . This value is small enough that the effects of the blockage on the jet attachment can be ignored. The test section terminates with an exit slot to atmospheric conditions  $48.7$  nozzle widths downstream of the orifice. Air is supplied by a  $100 \text{ psi}$  laboratory ring main via a mass flow controller (Omega FMA-2612A) upstream of the test section, which has an uncertainty of  $1.1\%$  at the operating mass flow rate,  $\dot{m} = 6.4 \text{ g/s}$ . The acoustic excitation is produced by a loudspeaker ( $60 \text{ W}$  Visaton SC 5) through an amplifier ( $40 \text{ W}$  Kemo Electronic M034N). The loudspeaker terminates the control port on the unattached side of the jet (a loudspeaker also terminates the attached side control port, but is not used in this paper). The carrier tone frequency used in all attached jet experiments is  $f_c = 2.5 \text{ kHz}$ , and the mean nozzle velocity is  $73.8 \pm 0.9 \text{ m/s}$ , which has a corresponding Reynolds number given by  $\text{Re}_{D_h} = uD_h/\nu \approx 5.3 \times 10^4$ , where  $D_h$  is the hydraulic diameter of the nozzle.

In Fig. 2, the jet emerges from the nozzle and attaches to the wall because of the Coandă effect.<sup>13</sup> A separation bubble is formed between the jet and the attachment wall, and a shear layer exists on the unattached side. The acoustic excitation increases the entrainment rate because it enhances the vorticity,<sup>1</sup> which reduces the pressure on either side of the jet. When the excitation is directed at the unattached side of the jet, the pressure reduction in the shear layer is greater than in the separation bubble. Mair *et al.*<sup>14</sup> used LES results to demonstrate that this is a result of a



FIG. 3. Photograph of attached jet test section.

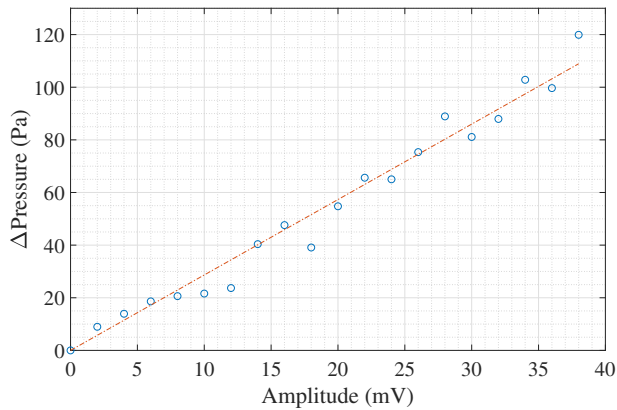


**FIG. 4.** Linearity curve for attached jet experiment at  $\dot{m} = 6.4$  g/s,  $f = 2.5$  kHz: change in mean pitot pressure against excitation amplitude with line of best fit overlaid. Pearson's correlation coefficient is  $\rho_r = 0.987$ .

biased increase in entrainment. The effect of the uneven pressure change is a reduction in the magnitude of the pressure difference across the jet, and hence a weakening of jet attachment strength and a downstream movement of the attachment point. This is reflected in the pitot probe signal, which has a positive, monotonic relationship with the excitation amplitude. This relationship is illustrated in Fig. 4, which shows the change in pressure measured by the pitot probe relative to the unexcited value plotted against the amplitude of the 2.5 kHz excitation tone, with a line of best fit plotted on top. Deviations from the line are within 12% of the span of the line, and the Pearson correlation coefficient is  $\rho_r = 0.987$ .

When excited with a constant tone, the jet attachment point moves downstream to a new steady state. Varying the amplitude of the acoustic excitation tone with a modulation signal causes a variation in the jet position—the jet responds at the modulating signal frequency.<sup>3</sup> The signals are sketched in Fig. 5, which shows an amplified AM input signal driving the loudspeaker, then being demodulated by the shear layer. The shear layer output is scaled in magnitude and shifted in phase by the jet dynamics, before being measured and sampled.<sup>5</sup> The jet position pitot measurement is used as an analogue to indicate the degree of jet spreading and hence the shear layer vortical response. Note that the presence of the jet dynamics in the attached jet experiment is the principal difference when compared with the free jet experiment, where the shear layer response is measured directly using PIV.

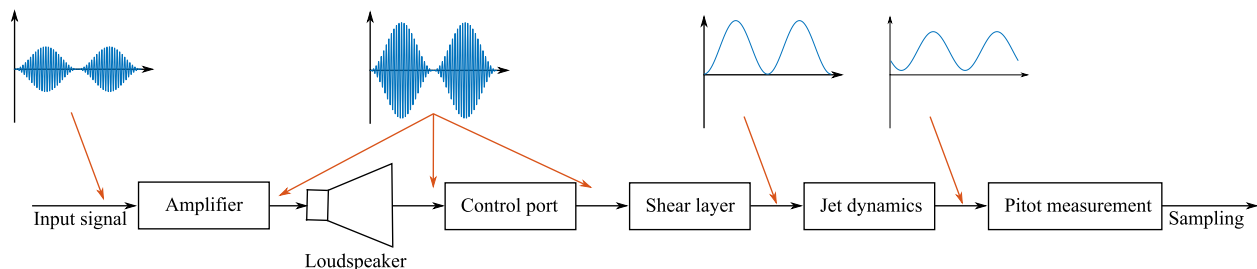


**FIG. 5.** Attached jet system block diagram.

### III. SIGNAL PROCESSING PERSPECTIVE

We assume in all experiments that the acoustic perturbations produced by the loudspeakers are large enough to dominate the shear layer and cause the vortex shedding to “lock on” to the excitation frequency.<sup>1</sup> Another assumption is that the strength of the vortices produced is modulated by the amplitude of the excitation during their creation, which was observed by Yehoshua and Seifert<sup>9</sup> and Nicholls *et al.*<sup>2</sup> The shear layer response to a constant input tone,

$$u_{SL} = B \sin(2\pi f_c t), \quad (1)$$

is depicted in Fig. 6(a), which shows the carrier signal (blue), the signal that modulates its amplitude (red), the resulting amplitude modulation (AM) signal that excites the jet (yellow), the vortex train produced in the shear layer in response (purple), and the vorticity of the vortex train that would be measured at a point in the shear layer (green). The size of each vortex sketched in the figure was calculated by taking the mean value of the modulating signal during the negative half of each carrier signal period. This was an arbitrary choice—using any fraction of the carrier period would work. Our experiments indicate that opposite-sense vortices are never created in the other half of the carrier period because of the natural vorticity offset in the shear layer. As in Nicholls *et al.*,<sup>2</sup> we model the vorticity signal as the half-wave rectified AM excitation signal. This model describes how the vortices redistribute the shear layer vorticity—a comparison of the vortex train and the vorticity signal in Fig. 6(b) demonstrates this.

When the amplitude of the carrier signal is modulated, the input signal becomes

$$u_{SL} = g_c(t)g_m(t) = \sin(2\pi f_c t)[A \sin(2\pi f_m t) + B], \quad (2)$$

which has  $g_m(t) \geq 0$  for  $A \leq B$ . In the limiting case, the AM signal is 100% modulated when  $A = B$ . The shear layer response in this case is shown in Fig. 6(b), which shows how the envelope of both the vortex train and the corresponding vorticity signal follow the modulating signal.

When  $A > B$ , the AM signal is overmodulated and  $g_m(t) < 0$  for some portion of the modulating period. During this portion, the phase of the carrier tone changes by  $180^\circ$ . However, the shear layer is insensitive to the phase of the carrier signal. This result is demonstrated in Fig. 7(a), where the AM signal is 160% modulated—vortices are still produced when  $g_m(t) < 0$ , and hence, jet spreading is still enhanced. The extreme case of  $B = 0$ , that is, 200% modulation, is shown in Fig. 7(b). Here, the modulating signal is negative for half of its period. The frequency of the vortex train envelope is double that of the modulating signal. The only effect on the vortex train of the periodic,  $180^\circ$  phase



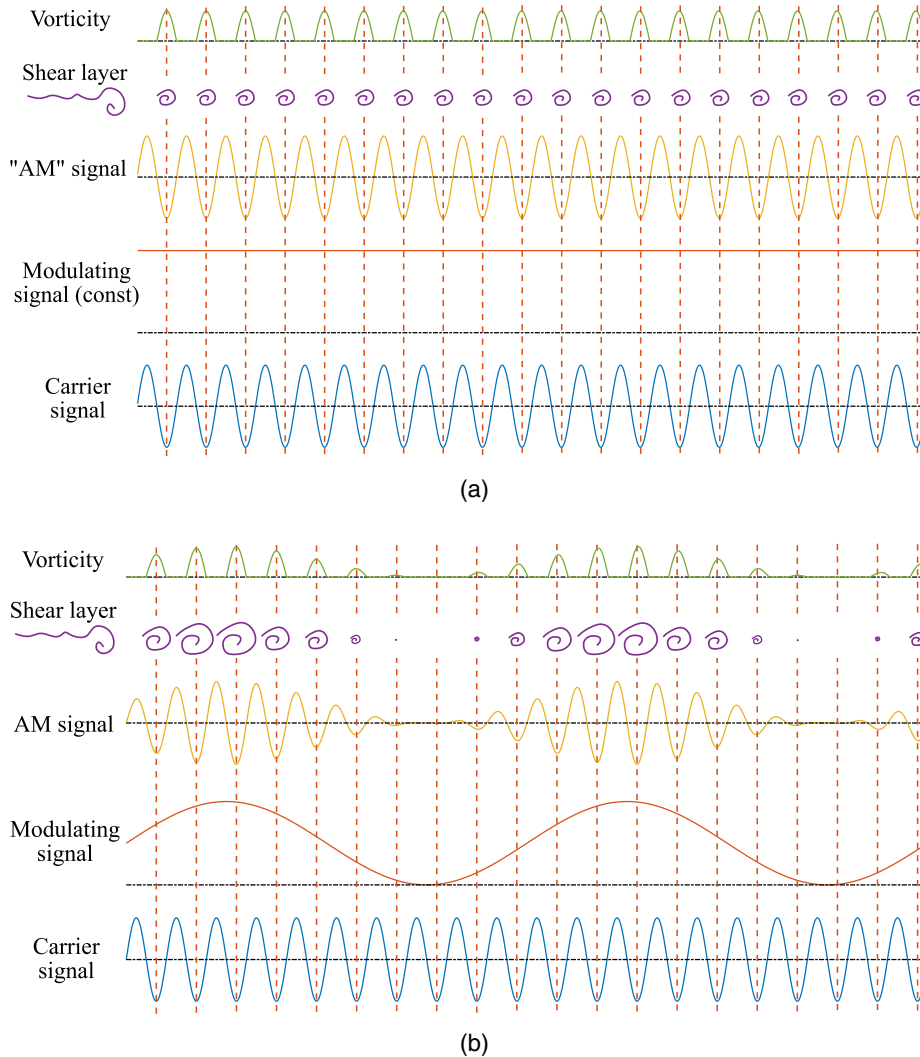


**FIG. 6.** Shear layer response to (a) constant carrier tone (i.e., constant modulation signal), and (b) 100% amplitude modulation (AM) signal. Reproduced with permission from Nicholls *et al.*, *Phys. Fluids* **34**, 115106 (2022). Copyright 2022 AIP Publishing. (a) Carrier tone with constant amplitude. (b) Carrier tone with 100% amplitude modulation.

change is the repeated vortex or absence of a vortex, as shown in Figs. 7(a) and 7(b), which corresponds to a periodic timing shift in vortex shedding. When the modulating signal goes negative, two vortices are produced with a time gap equal to half the carrier period. In the other direction, when the modulating signal goes positive, the time gap between vortices is equal to two carrier periods.

Both the phase-insensitivity and the demodulation effect can be summarized into a half-wave rectification operation, as used in Nicholls *et al.*<sup>2</sup> Without loss of generality, we assume full rectification for the purpose of quantitative analysis. Since we are interested in the relative power of the demodulated frequencies, both operations give identical results. The shear layer output, which is related to the vorticity and hence the jet spreading, is given by

$$y_{\text{SL}}(t) = |u_{\text{SL}}(t)| = |\sin(2\pi f_c t) [A h(f_c \pm f_m) \sin(2\pi f_m t) + B h(f_c)]|, \quad (3)$$

where  $h(f)$  represents the combined authority of the amplifier, loudspeaker, and control port as a function of the frequencies produced by

the loudspeaker, which for an AM signal are  $f_c \pm f_m$  and  $f_c$ . The effect of the rectification on the carrier signal,  $\sin(2\pi f_c t)$ , is that the power shifts from  $f_c$  to DC and harmonics of  $f_c$ . The output can be re-written as

$$y_{\text{SL}}(t) = [E + F \sin(2\pi 2f_c t) + \dots] |A h(f_c \pm f_m) \sin(2\pi f_m t) + B h(f_c)|, \quad (4)$$

where the modulus of the carrier sinusoid has been replaced with its Fourier series representation. The result is that the absolute value of the modulating signal term in (4) is mixed with DC and harmonics of  $f_c$ . It is assumed that there will be no response at the harmonics of  $f_c$  because the bandwidth of the jet dynamics is typically an order of magnitude below  $2f_c$ .<sup>5</sup> Note that the effect of the function  $h(f)$  is simply to adjust the modulation depth depending on the authority of the amplifier, loudspeaker, and control port at the frequencies  $f_c$  and  $f_c \pm f_m$ . Note also that the shear layer output is subject to the sampling operation described in Nicholls *et al.*<sup>2</sup> For the case when the modulating frequency is kept small ( $f_m \ll f_c/2$ ), the influence of both  $h(f)$  and

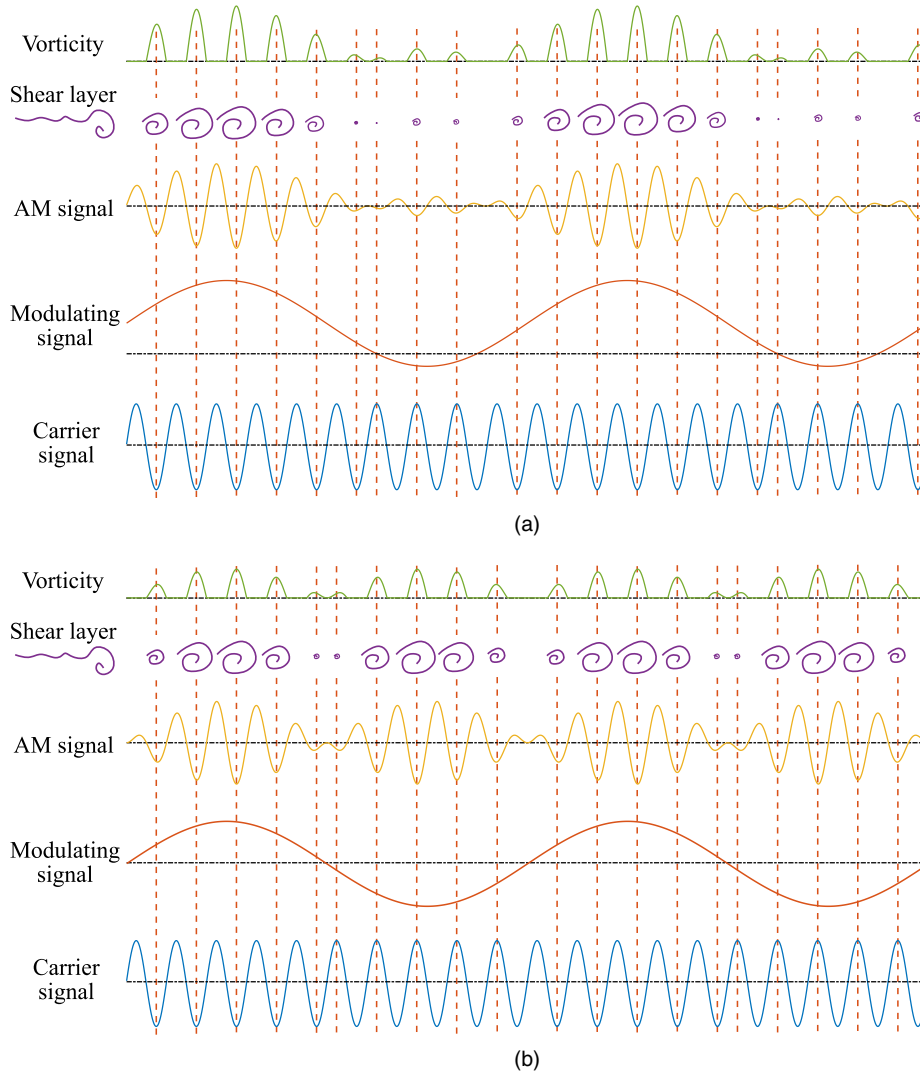


**FIG. 7.** Shear layer response to (a) 160% and (b) 200% amplitude modulation signals. (a) Carrier tone with 160% amplitude modulation. (b) Carrier tone with 200% amplitude modulation.

aliasing effects is avoided and as such,  $h(f_c) \approx h(f_c \pm f_m)$ . The constant,  $E$ , is applied to all terms, and since it is the relative amplitude of each term that is relevant, it is absorbed into  $h(f_c)$ . Applying these assumptions results in the shear layer output given by

$$y_{SL} = h(f_c \pm f_m) |A \sin(2\pi f_m t) + B|. \quad (5)$$

This expression demonstrates that the rectification has demodulated the excitation signal because the response is at baseband. The effect of the remaining modulus operation on (5) depends on the degree of modulation. When  $A \leq B$ , the modulus operation does nothing and the response is at  $f_m$ . When overmodulated ( $A > B$ ), a fraction of the power at the fundamental,  $f_m$ , is shifted to DC and harmonics of  $f_m$ , as was the case with the carrier tone in (4). In the 200% modulation case where  $B = 0$ , all power is removed from  $f_m$ .

Importantly, this transfer of power occurs at the shear layer link in the chain of signal processing events (Fig. 5) rather than before. In this case, the shear layer and jet respond primarily at DC and  $2f_m$ .

However, in terms of bandwidth requirements, the relevant frequency for  $h(f_c \pm f_m)$ —the response of the amplifier, loudspeaker, and control port—is  $f_m$ , and it is the shear layer nonlinearity that transfers the power away from the fundamental frequency. Under these assumptions, it follows from (5) that

$$y_{SL,200} = A h(f_c \pm f_m) |\sin(2\pi f_m t)|. \quad (6)$$

The Fourier series of this function is given by

$$y_{SL,200}(t) = A h(f_c \pm f_m) \left( \frac{2}{\pi} - \frac{4}{\pi} \sum_{n=1}^{\infty} \frac{1}{4n^2 - 1} \cos(2\pi(2nf_m)t) \right). \quad (7)$$

If the harmonics above  $2f_m$  are ignored, the resulting signal is given by

$$y_{SL,200} = A h(f_c \pm f_m) \left( \frac{2}{\pi} - \frac{4}{3\pi} \cos(2\pi 2f_m t) \right). \quad (8)$$

For comparison, if  $A = B$  (100% AM), (5) produces the standard demodulated response at  $f_m$  given by

$$\gamma_{SL,100} = A h(f_c \pm f_m)(1 + \sin(2\pi f_m t)), \quad (9)$$

so that the ratio of the power at the demodulated response frequency between the two cases is  $20 \log_{10}(4/3\pi) = -7.44$  dB. The response function at the demodulated frequency has gone from a positive sine in the 100% AM case in (9) to a negative cosine in the overmodulated case in (8), a phase shift of  $-90^\circ$ . Hence, overmodulating doubles the shear layer response frequency but reduces the response power and shifts the response phase. However, this 7.44 dB ratio is not strictly a “fair” comparison because the input power is not the same in both cases—the 200% AM input differs only by setting  $B = 0$ . If the amplitude of the side bands at  $f_c \pm f_m$  in the 200% AM input is increased to match the total input power of the 100% case, then the resulting power ratio is

$$P_{2f_m} = P_{f_m} - 2.67 \text{ dB}. \quad (10)$$

To summarize, the rectification model has made several predictions about the shear layer response when the excitation waveform amplitude is overmodulated. We focus here on the 200% modulation case relative to the 100% case.

1. The envelope frequency of the vortex train is doubled.
2. There is a periodic shift in the timing of the vortex shedding corresponding to the zero-crossings of the modulating signal [Fig. 7(b)].
3. The magnitude at the demodulated response frequency (now at  $2f_m$ ) reduces by either 7.44 dB (simply set  $B = 0$ ) or 2.67 dB (match 100% AM input power).
4. The phase at the demodulated frequency is shifted by  $-90^\circ$ .

#### IV. RESULTS: FREE, ROUND JET

A subset of the data presented in this section are baseline results that were published in Nicholls *et al.*<sup>2</sup> and are reproduced in Fig. 8, Fig. 9, and Figs. 10(a) (Multimedia view), 10(c), and 10(e), for ease of comparison.

The unexcited free jet with a flow rate of 1.06 g/s was sampled for 250 PIV frames at 10 Hz. An example of a raw PIV image is shown in Fig. 8. The vorticity of the time-averaged flow field is shown in Fig. 9(a). This figure illustrates the off-perpendicular orientation of the jet

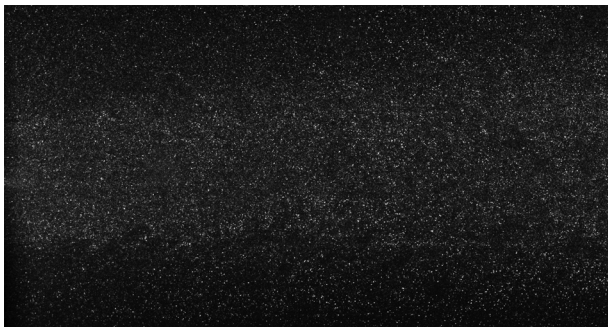


FIG. 8. Example raw image of unexcited free jet. Reproduced with permission from Nicholls *et al.*, Phys. Fluids **34**, 115106 (2022). Copyright 2022 AIP Publishing.

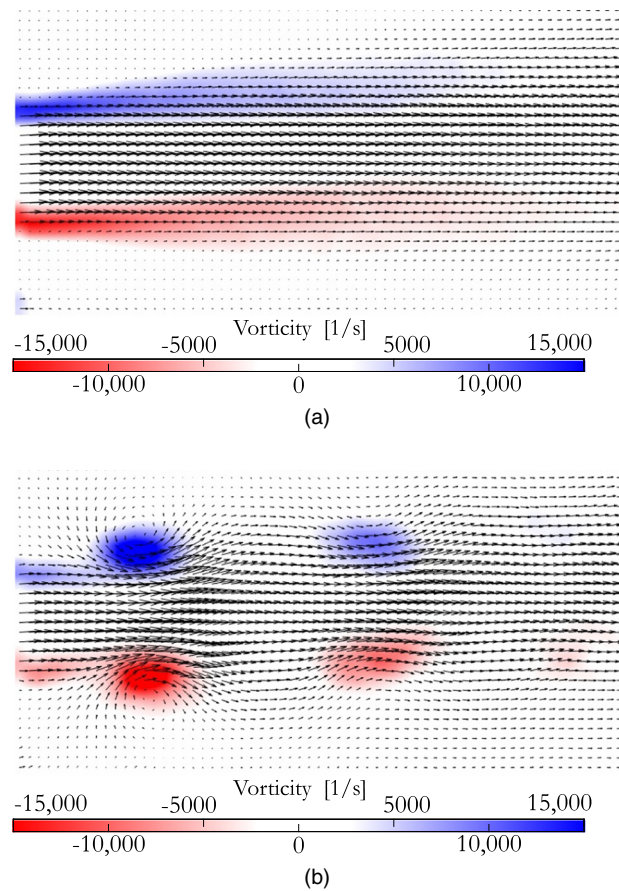
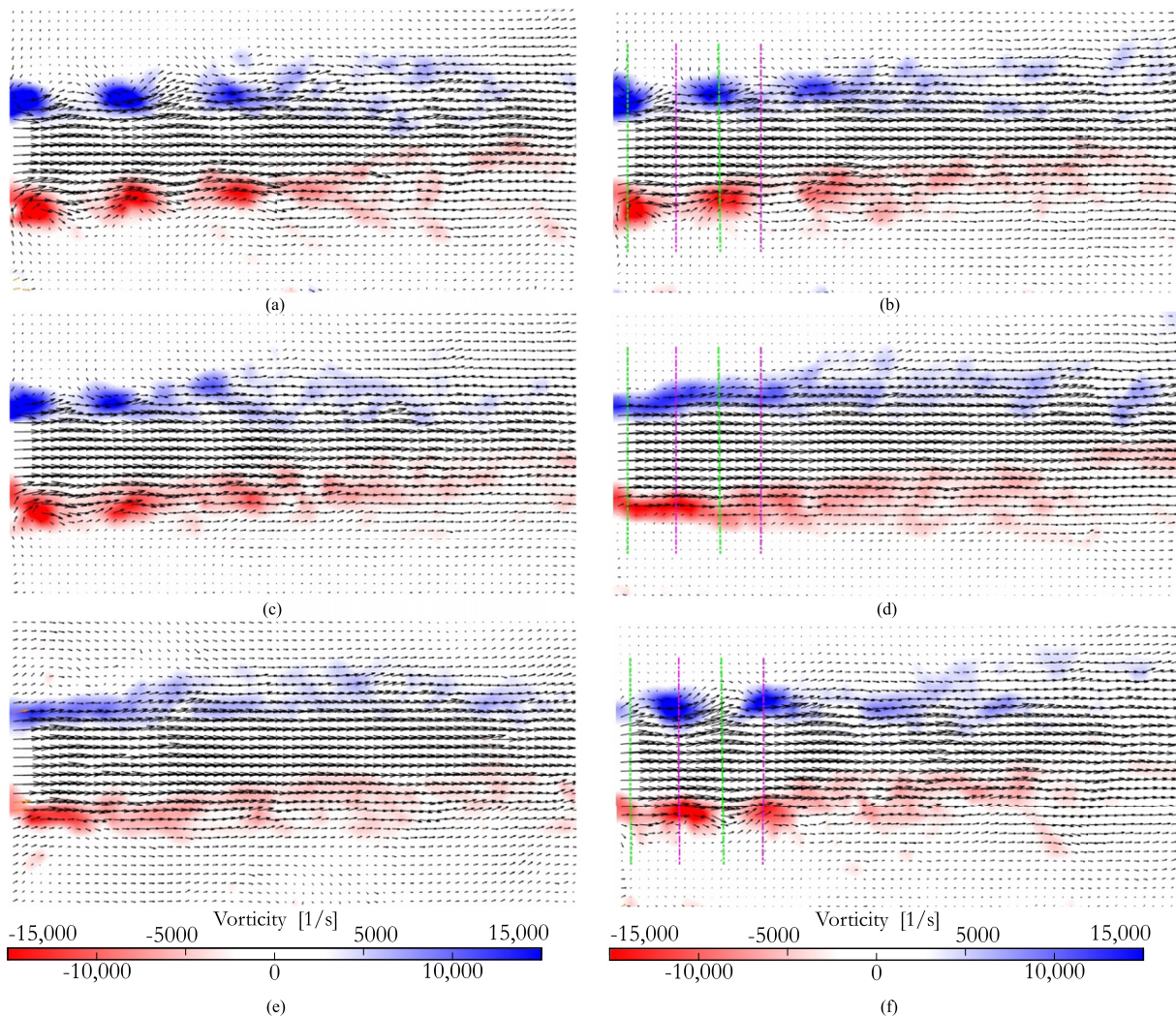


FIG. 9. Vorticity of time-averaged free jet: (a) unexcited and (b) 1 kHz excitation. Reproduced with permission from Nicholls *et al.*, Phys. Fluids **34**, 115106 (2022). Copyright 2022 AIP Publishing. (a) Vorticity of time-averaged, unexcited free jet. (b) Vorticity of phase-averaged free jet with 1 kHz excitation.

described in Sec. II. The jet does not come close to the sides of the box, so the angle has a negligible effect on the results. There are no coherent structures in the flow field because the time averaging has removed any that might have been present. This is because the natural vortex shedding frequency is not a multiple of the triggering frequency so is aliased onto a frequency other than DC. For comparison, Fig. 9(b) shows the vorticity of the phase-averaged flow field ( $N = 100$  PIV frames) where the upstream loudspeaker was exciting the flow with a constant amplitude tone at 1 kHz. The vorticity field shows a 2D slice through vortex rings that are generated at a multiple of the triggering frequency. In this case, the lock-on effect has clearly been achieved, with the vortices shed at the excitation frequency. A more quantitative assessment of this flow field is given in Nicholls *et al.*<sup>2</sup>

An experiment was conducted with  $f_c = 2020$  Hz,  $f_m = 0.5$  Hz, and 100% modulation [ $B = A$  in (2)]. This corresponds to the case depicted in Fig. 6(b). This carrier was chosen because the shear layer showed a strong response when excited at this frequency. As a comparison, an experiment was conducted with the same carrier frequency and the modulating frequency set to  $f_m = 0.25$  Hz with 200% modulation [ $B = 0$  in (2)]. This corresponds to the case depicted in Fig. 7(b).





**FIG. 10.** Vorticity of ensemble-averaged flow fields with  $f_c = 2020$  Hz: left [(a), (c), and (e)], reproduced Nicholls *et al.*, Phys. Fluids 34, 115106 (2022). Copyright 2022 AIP Publishing.<sup>2]</sup>  $f_m = 0.5$  Hz with 100% modulation ( $B = A$  in (2)); right [(b), (d), and (f)],  $f_m = 0.25$  Hz with 200% modulation [ $B = 0$  in (2)]; at several points in the phase. Subfigures (a), (c), and (e) reproduced with permission from Nicholls *et al.*, Phys. Fluids 34, 115106 (2022). Copyright 2022 AIP Publishing. (a) Maximum vortex strength, 100% AM. (b) Vortex train position for first half of modulating period, 200% AM. (c) Intermediate vortex strength, 100% AM. (d) Modulating signal zero-crossing, 200% AM. (e) Minimum vortex strength, 100% AM. (f) Vortex train position for second half of modulating period, 200% AM. Linked animations are periodic and should be played on repeat. Multimedia views: [for (a), (c), and (e)], <https://doi.org/10.1063/5.0130336.1>; [for (b), (d), and (f)], <https://doi.org/10.1063/5.0130336.2>

An ensemble of five sets of 20 points ( $f_m = 0.5$  Hz, 100% AM) and 40 points ( $f_m = 0.25$  Hz, 200% AM) through the phase of the modulating period was produced, respectively. Figure 10 shows the ensemble-averaged (phase-averaged) vorticity field at three salient points in the phase of the modulating signal in each experiment—the 100% AM case on the left, and 200% AM on the right. For the 100% AM data, Fig. 10(a) shows a time when the modulating signal is around its maximum value so that a strong vortical response is observed in the shear layer. Similarly, Fig. 10(e) shows a point in the phase where the modulating signal is close to zero and the response shows no coherent vortical structures. A point between these extremes is shown in Fig. 10(c). An animation is linked in the caption of Fig. 10.

For the 200% AM data on the right in Fig. 10, it is not possible to determine the sign of the modulating signal during each half of its period because the trigger generator does not time the signal generator, so they are referred to as the first and second halves. Figure 10(b) (Multimedia view) shows a typical vorticity field during the first half of the modulating period. The vortex train temporal phase can be judged from the locations of each vortex ring because the vortex generation frequency has been aliased to DC by the under-sampling. In this case, the timing of vortex shedding results in alignment with the green lines added to the image. Conversely, during the second half of the modulating period in Fig. 10(f), the vortices align with the pink lines. Figure 10(d) shows the zero-crossing of the modulating signal, which

shows no coherent vortical structures and resembles the 100% AM minimum response case in Fig. 10(e). An animation of the 200% AM data is linked in the caption of Fig. 10.

## V. RESULTS: ATTACHED JET

The purpose of the attached jet experiments is to validate the quantitative aspect of the rectification model presented in Sec. III, as

well as providing an example application to illustrate how overmodulation can be harnessed as an excitation technique.

An experiment was conducted where the loudspeaker was excited with an AM signal [see (2)] with a modulating frequency of  $f_m = 5$  Hz,  $A = 20$  mV, and  $B = 0$  (200% AM). The power spectral density of the data sampled from the pitot probe measurement was computed to give the spectrum shown in Fig. 11. Detail around  $2f_m$  is

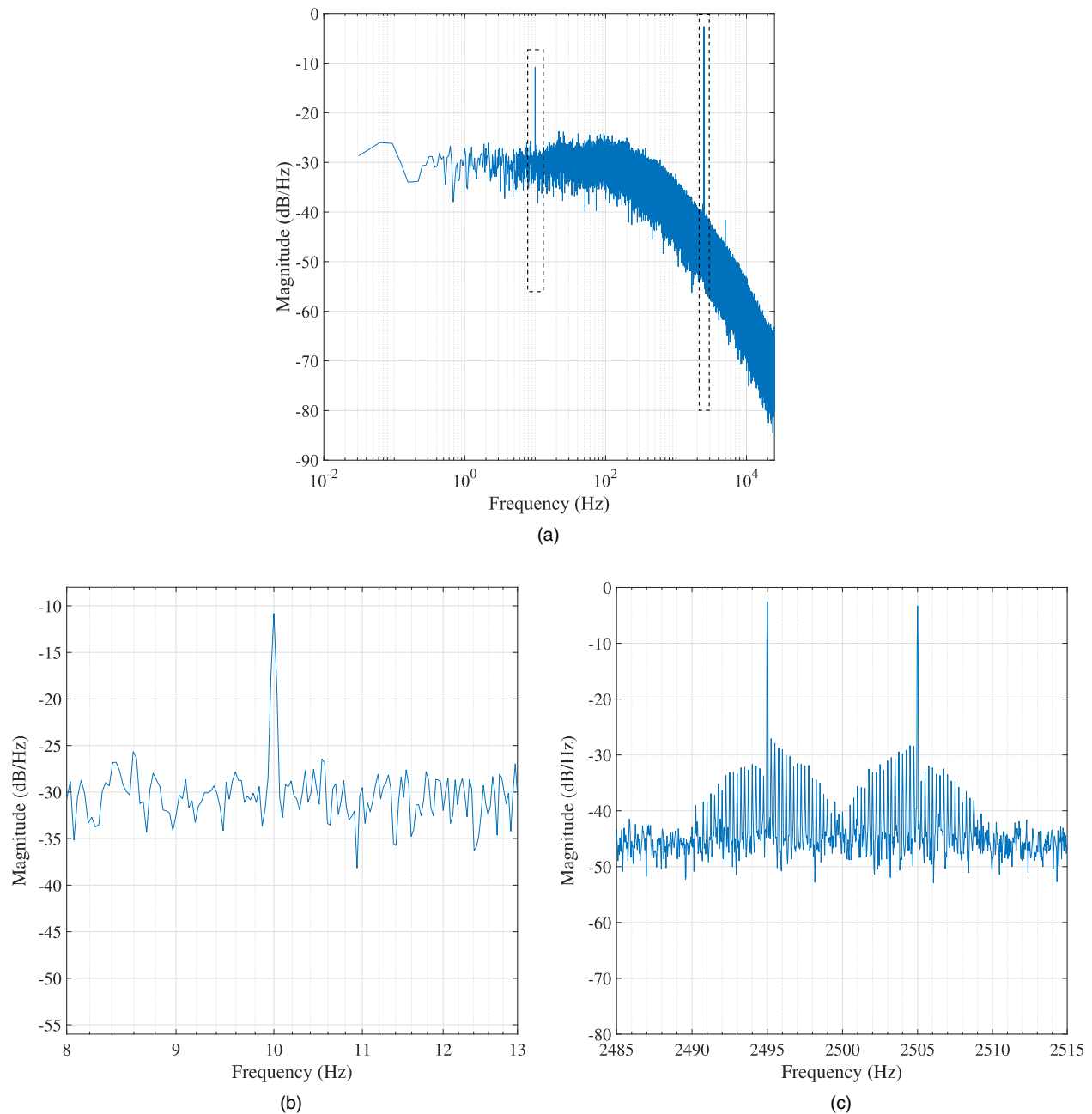


**FIG. 11.** Power spectral density of pitot probe signal at  $\dot{m} = 6.4$  g/s with overmodulated input:  $f_c = 2.5$  kHz,  $f_m = 5$  Hz,  $A = 20$  mV, and  $B = 0$  (200% AM). (a) Full spectrum. (b) Zoom on  $2f_m = 10$  Hz. (c) Zoom on  $f_c = 2500$  Hz.

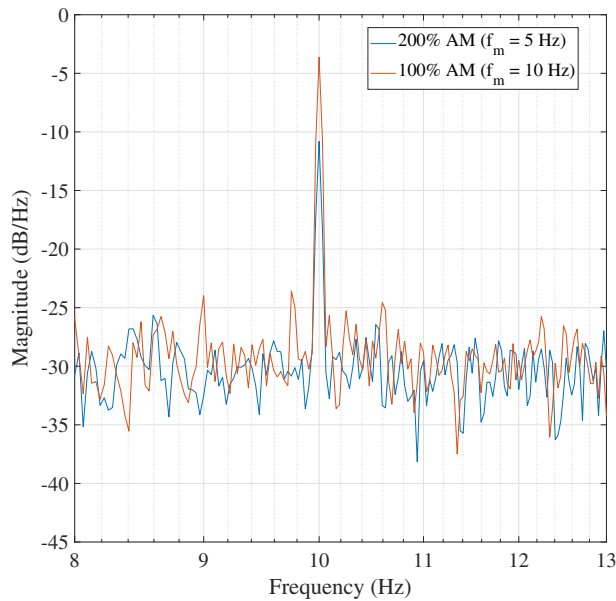


**FIG. 12.** Power spectral density of pitot probe signal at  $\dot{m} = 6.4$  g/s,  $f_c = 2.5$  kHz: 100% AM,  $f_m = 10$  Hz,  $A = B = 20$  mV (red), and 200% AM,  $f_m = 5$  Hz,  $A = 20$  mV,  $B = 0$  (blue).

shown in Fig. 11(b), while the direct measurement of the acoustic input tones at  $f_c \pm f_m$  by the pitot is highlighted in Fig. 11(c). These data demonstrate the frequency doubling of the jet response to an overmodulated input signal—the response is observed at  $2f_m = 10$  Hz.

Experiments were conducted to validate the calculations in Sec. III on the predicted power in the demodulated response at  $2f_m$  with an overmodulated input relative to the power at  $f_m$  with a 100% modulation input. Modulating frequencies  $f_m = 2, 5, 10, 20$ , and  $40$  Hz were used in separate experiments at 100% modulation with  $A = B = 20$  mV, which was repeated at 200% AM with  $f_m = 1, 2.5, 5, 10$ , and  $20$  Hz and  $A = 20$  mV,  $B = 0$ . Choosing low values for  $f_m$  ensures that  $h(f_c \pm f_m)$ , the authority of the amplifier, loudspeaker and control port as a function of frequency, does not vary significantly between the 100% and 200% cases. A comparative example of the power spectral densities of the pitot probe measurements from the  $f_m = 10$  Hz (100% AM) and  $f_m = 5$  Hz (200% AM) experiments is shown in Fig. 12. The response power of all of the data is summarized in Table I. The final

**TABLE I.** Magnitude response comparison: 100% and 200% modulation at several values of  $f_m$ .

Response frequency (Hz)	Magnitude, 100% AM (dB)	Magnitude, 200% AM (dB)	Magnitude ratio (dB)
2	−5.16	−11.58	6.42
5	−4.10	−11.63	7.53
10	−3.62	−10.81	7.19
20	−2.15	−10.04	7.89
40	−1.38	−9.68	8.30
Average ratio (dB)			$7.49 \pm 0.71$

row shows the average amplitude ratio to give a power ratio of  $7.49 \pm 0.71$  dB, cf. the calculated value of 7.44 dB in Sec. III.

As a further demonstration of the validity of the analysis in Sec. III, the jet dynamic response was measured up to 500 Hz using  $f_c = 2.5$  kHz. This consisted of setting a value of  $f_m$ , measuring the response with the pitot, computing the power spectral density, and extracting its value at the expected response frequency ( $f_m$  for 100%,  $2f_m$  for 200%). This was done once for the 100% modulation case with  $20 \leq f_m \leq 500$  Hz, and twice with  $10 \leq f_m \leq 250$  Hz for the 200% modulation case. The input amplitudes were  $A = B = 20$  mV for the 100% AM case, and  $A = 20$  mV and  $A = 20\sqrt{3} = 34.64$  mV,  $B = 0$  for each of the overmodulation cases. The first overmodulation case was conducted to demonstrate the predicted  $-7.44$  dB drop relative to the 100% AM case. However, as expected, the uncertainty in the resulting curves is relatively large because the measured response has a lower signal-to-noise ratio than the 100% AM case. Therefore, the second overmodulation case was performed with the total input power equal to the 100% AM case, as proposed in Sec. III, to demonstrate that the technique can produce data with comparable uncertainty, but still using only half of the required input bandwidth. The resulting responses are shown in Fig. 13, along with the 100% AM magnitude response shifted by both  $-7.44$  dB (cf. first overmodulation case) and  $-2.67$  dB (cf. second overmodulation case), and its phase response shifted by  $-90^\circ$ . These are the predicted magnitude and phase shifts calculated in Sec. III.

## VI. DISCUSSION

Figure 10 offers a direct comparison between the response of the flow field to 100% and 200% AM waveforms to illustrate the effect of an overmodulated input signal. The 100% AM data in Fig. 10 agree

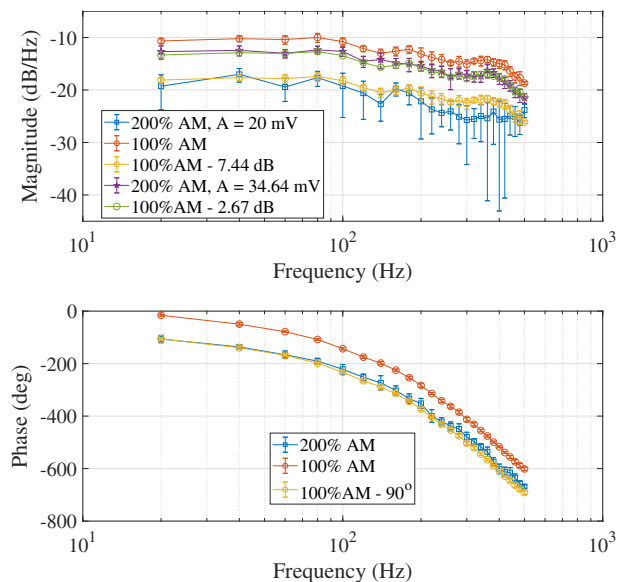


**FIG. 13.** Jet dynamic responses at  $\dot{m} = 6.4$  g/s,  $f_c = 2.5$  kHz: 200% AM with  $A = 20$  mV (blue, squares), 100% AM (red, circles), 100% AM shifted by  $-7.44$  dB and  $-90^\circ$  (yellow, stars), 200% AM with  $A = 20\sqrt{3} = 34.64$  mV for input power equality (purple, stars, magnitude only), and 100% AM shifted by  $-2.67$  dB (green, circles, magnitude only). Error bars show 1 standard deviation from the mean.



with the corresponding sketch in Fig. 6(b)—the vortex strength follows the modulating signal, varying between an unexcited flow field and the maximum strength vortex train once per modulating period. There is also an agreement between the overmodulated data on the right of Fig. 10 and the corresponding sketch in Fig. 7(b). The effect of the zero-crossing of the modulating signal predicted in Sec. III—either half or double the usual time gap between vortices—is observed as a periodic shift in the vortex positions. Since the phase of the modulating signal in the experiment was not known, the first and second halves of the modulating period were simply determined from the observed vortex train positions and the weak vortical response during the zero-crossing. In the 100% case on the left of Fig. 10, the vortex train position does not change because the modulating signal is always positive (or zero) as in Fig. 6(b). The frequency doubling effect in the overmodulated case is apparent in the experimental data—the envelope of the vortex train varies between the unexcited flow field and the maximum strength vortex train (either green or pink) twice in one period of the modulating signal, whereas it only happens once in the 100% case.

The results in Sec. V represent a quantitative verification of the rectification model presented in Sec. III. Figure 12 illustrates a direct spectral comparison between the shear layer responses to 200% and 100% AM excitation. The modulating frequency for the 200% AM excitation signal (5 Hz) is half that of the 100% AM signal (10 Hz). The spectra show the demodulated shear layer response is at 10 Hz in both cases, exemplifying the frequency-doubling effect of the shear layer on an overmodulated excitation signal. The relative magnitudes of the demodulated responses illustrate the predicted magnitude shift. Table I shows that the power at the expected response frequency reduces by a mean value of 7.49 dB when the input is changed from 100% AM to 200% AM by simply removing the carrier tone from the excitation signal. This closely matches the magnitude shift predicted by the analysis of the rectification model, which is 7.44 dB. Figure 13 shows the measured jet response to 100% and 200% AM inputs at several frequencies. The 100% AM magnitude response shifted by 2.67 dB is in close agreement with the 200% AM response where the input power is equal. Similarly, the 90° phase shift predicted by the model is well-illustrated in the phase response. Between the free jet and attached jet experiments, all predictions made by the model in Sec. III have been substantiated.

Overmodulating an input waveform has applications beyond the validation of the rectifier model presented here. The key to its usefulness is that the change in frequency from  $f_m$  to  $2f_m$  occurs in the shear layer, after the actuator (Fig. 5). This means that the actuator bandwidth is effectively doubled. Ignoring the response at the harmonics of  $2f_m$ , the penalty is a 2.7 dB reduction in response power. This may have application in several contexts where harmonic excitation is used, for example, in flow control applications where a resonant actuator or an acoustic cavity with a sharp, narrow bandwidth is employed to excite a flow. In these cases, it is desirable to amplify a relatively narrow range of frequencies to maximize the authority of the actuator—that is, make  $h(f)$  large across a small range of frequencies. Examples in the literature include the cantilevered piezoelectric devices used by Wiltse and Glezer<sup>3</sup> and Cattafesta *et al.*<sup>15</sup> or the ultrasonic transducers used by Mair and Bacic<sup>16</sup> and Mair *et al.*<sup>17</sup> In all of these cases, the actuators have a highly selective frequency response. However, if the device in question is to be used dynamically, the system frequency

response may be limited by the bandwidth of the actuator-cavity resonance— $h(f_c \pm f_m)$  rolls off as  $f_m$  increases. Wiltse and Glezer<sup>3</sup> commented that this limits the achievable value of  $f_m$  in their case. If overmodulation is used, the bandwidth is doubled because the conversion from  $f_m$  to  $2f_m$  occurs *after* the actuator-cavity stage of the system, as illustrated in Fig. 5.

As another example, when identifying jet dynamics, it is desirable to keep  $h(f_c \pm f_m)$  in a flat region to avoid confusing the magnitude response of the jet with the roll-off of the actuator. Jet dynamics have been identified experimentally for the purpose of controller design.<sup>5,8</sup> Flat, “well-behaved” regions of actuator bandwidth can be extended by a factor of 2 using the overmodulation technique. We have demonstrated this in Sec. V—the data in Fig. 13 constitute the frequency response of the attached jet dynamics.

In any application, implementing overmodulated excitation requires changes to be made to the excitation signal alone. As such, it can be readily applied to existing actuation hardware without inconvenience.

## VII. SUMMARY AND CONCLUSIONS

This paper has employed the signal processing perspective developed by Nicholls *et al.*<sup>2</sup> to investigate the effects of overmodulated acoustic excitation on jet shear layer behavior. We have demonstrated that the half-wave rectification model proposed in Nicholls *et al.*<sup>2</sup> is an accurate description of the shear layer response with analysis and experiments. We have also shown that overmodulating the amplitude of an input carrier waveform results in a demodulated response principally at double the modulating frequency, an outcome predicted by the model that represents a practical excitation technique. A periodic, 180° phase shift in the shear layer response was also predicted by the model, resulting from the zero-crossings of the modulating signal. Both the phase shift and frequency doubling were verified experimentally by acoustically exciting a free, round jet and studying it using PIV. The phase shift was observed as a shift in vortex train timing, while the frequency doubling was seen in the vortex train envelope relative to the 100% AM case.

A second experimental setup was employed involving an acoustically excited jet emerging from a nozzle and attaching to a setback, inclined wall. A downstream pitot probe gave an indication of the jet position, which provided a proxy for the shear layer response. This setup was used to demonstrate the validity of the quantitative elements of the rectification model, as well as providing an example application for overmodulation as an excitation technique. The data confirmed the predicted magnitude and phase shifts at the demodulated frequency.

The principal conclusion of this paper is that the half-wave rectification model proposed in Nicholls *et al.*<sup>2</sup> is an accurate description of the operation of a shear layer in response to acoustic excitation. A complete model should also include the sampling action demonstrated in our previous work.<sup>2</sup> Through the lens of signal processing, a shear layer behaves like a demodulator in the form of an envelope detector implemented by a half-wave rectifier, followed by a digital sampler.

The second outcome of this paper is that the frequency doubling that occurs in the shear layer when the input waveform is overmodulated can be harnessed to yield a doubling of the effective actuator bandwidth at the cost of a 2.7 dB reduction in the demodulated response power. Implementation requires changes only to the



excitation signals rather than the actuation hardware. The technique is expected to be useful in flow control applications where a harmonic excitation signal is required and for the identification of flow dynamics for the purpose of closed-loop control.

## ACKNOWLEDGMENTS

The authors gratefully acknowledge the support of this work by the EPSRC program grant (No. EP/P000878/1). We thank the reviewers and editor for their valued contributions to the paper.

## AUTHOR DECLARATIONS

### Conflict of Interest

The authors have no conflicts to disclose.

### Author Contributions

**Chris James Nicholls:** Conceptualization (lead); Data curation (lead); Formal analysis (lead); Investigation (lead); Methodology (equal); Writing – original draft (lead); Writing – review & editing (lead). **Kharthik Chakravarthy:** Data curation (equal); Formal analysis (supporting); Methodology (lead); Writing – review & editing (supporting). **Brian Ming Tak Tang:** Formal analysis (supporting); Writing – review & editing (supporting). **Benjamin Williams:** Funding acquisition (equal); Resources (lead). **Marko Bacic:** Formal analysis (supporting); Funding acquisition (lead); Writing – review & editing (supporting).

## DATA AVAILABILITY

The data that support the findings of this study are available from the corresponding author upon reasonable request.

## REFERENCES

- <sup>1</sup>S. C. Crow and F. H. Champagne, “Orderly structure in jet turbulence,” *J. Fluid Mech.* **48**, 547–591 (1971).
- <sup>2</sup>C. J. Nicholls, K. Chakravarthy, B. M. T. Tang, B. A. O. Williams, and M. Bacic, “On acoustically modulated jet shear layers and the Nyquist–Shannon sampling theorem,” *Phys. Fluids* **34**, 115106 (2022).
- <sup>3</sup>J. M. Wiltse and A. Glezer, “Manipulation of free shear flows using piezoelectric actuators,” *J. Fluid Mech.* **249**, 261–285 (1993).
- <sup>4</sup>S. A. Jacobson and W. C. Reynolds, “Active control of streamwise vortices and streaks in boundary layers,” *J. Fluid Mech.* **360**, 179–211 (1998).
- <sup>5</sup>C. J. Nicholls and M. Bacic, “Closed-loop control of a piezo-fluidic amplifier,” *AIAA J.* **58**, 2414–2427 (2020).
- <sup>6</sup>C. Nicholls and M. Bacic, “Fluidic oscillator with active phase control,” in *AIAA SciTech 2022 Forum* (AIAA, San Diego, CA, 2022).
- <sup>7</sup>B. L. Smith and A. Glezer, “Jet vectoring using synthetic jets,” *J. Fluid Mech.* **458**, 1–34 (2002).
- <sup>8</sup>I. Rapoport, D. Fono, K. Cohen, and A. Seifert, “Closed-loop vectoring control of a turbulent jet using periodic excitation,” *J. Propul. Power* **19**, 646–654 (2003).
- <sup>9</sup>T. Yehoshua and A. Seifert, “On the evolution of amplitude modulated excitation in still air,” *Int. J. Flow Control* **3**, 171 (2011).
- <sup>10</sup>B. Vukasinovic, D. Lucas, and A. Glezer, “Direct manipulation of small-scale motions in a plane shear layer,” AIAA Paper No. 2004-2617 (2004).
- <sup>11</sup>B. P. Lathi and D. Zhi, *Modern Digital and Analog Communication Systems* (Oxford University Press, Inc., 1995).
- <sup>12</sup>H. Nyquist, “Certain topics in telegraph transmission theory,” *Trans. Am. Inst. Electr. Eng.* **47**, 617–644 (1928).
- <sup>13</sup>H. Coandă, “Device for deflecting a stream of elastic fluid projected into an elastic fluid,” US Patent 2,052,869 (April 19, 1936).
- <sup>14</sup>M. Mair, M. Bacic, and P. Ireland, “On dynamics of acoustically driven bistable fluidic valves,” *J. Fluids Eng.* **141**, 061202 (2019).
- <sup>15</sup>L. Cattafesta III, S. Garg, M. Choudhari, and F. Li, “Active control of flow-induced cavity resonance,” AIAA Paper No. 97-1804 (1997).
- <sup>16</sup>M. Mair and M. Bacic, “Fluid dynamics of a bistable diverter under ultrasonic excitation—Part I: Performance characteristic,” *J. Fluids Eng.* **143**, 071201 (2021).
- <sup>17</sup>M. Mair, M. Bacic, K. Chakravarthy, and B. Williams, “Fluid dynamics of a bistable diverter under ultrasonic excitation—Part II: Flow visualization and fundamental mechanisms,” *J. Fluids Eng.* **143**, 071202 (2021).